ROYAL SOCIETY OF CHEMISTRY

Journal Name

ARTICLE

Hierarchical Nanosheet-constructed Yolk-shell TiO$_2$ Porous Microspheres for Lithium Batteries with High Capacity, Superior Rate and Long Cycle Capability

Jun Jin,[a] Shao-Zhuan Huang,[a] Yu Li,[a, *] He Tian,[b] Hong-En Wang,[a] Yong Yu,[a] Li-Hua Chen,[a] Tawfique Hasan[c] and Bao-Lian Su[a, d, e, *]

A hierarchical nanosheet-constructed yolk-shell TiO$_2$ (NYTiO$_2$) porous microsphere is synthesized through a well designed one-pot template-free solvothermal alcoholysis process using tetraethylenepentamine (TEPA) as the structure directing reagent. Such yolk-shell structure with a highly porous shell and dense mesoporous core is quite advantageous as an anode material for lithium ion batteries (LIBs). The outer, 2D nanosheet-based porous (15 nm) shell and the nanocrystal-based inner mesoporous (3 nm) core provide a stable, porous framework, effective grain boundaries and short diffusion pathway for Li$^+$ and electron transport, facilitating lithium insertion/extraction. The voids between the core and the shell can not only store the electrolyte due to capillary and facilitate charge transfer across the electrode/electrolyte interface but also buffer the volume change during the Li$^+$ insertion/extraction. As a result, NYTiO$_2$ demonstrates excellent Li$^+$ capacity with outstanding cycle performance and superior rate capability at different rates for >700 cycles, retaining a 225 mA h g^{-1} reversible capacity after 100 cycles at 1 C. In partcular, the reversible capacity can still be maintained at 113 mA h g^{-1} after 100 cycles at 10 C. We also observe the formation of homogeneously distributed 5~10 nm Li$_2$Ti$_2$O$_4$ nanocrystallites on the surface of the nanosheets upon discharge-charge process. The synergy of the yolk-shell structure with dual mesopores in shell and core and the Li$_2$Ti$_2$O$_4$ nanocrystallites endow the hierarchical NYTiO$_2$ with high reversible capacity, excellent rate capability and outstanding cycle performance.

1. Introduction

Rechargeable lithium ion batteries (LIBs) have attracted much attention due to their high-power energy applications, ranging from portable electronics and consumer devices to electric vehicles and large-scale grid energy storage.[1-3] However, the use of LIBs for high-power application is often limited by the safety and kinetic problems associated with the electrode materials, such as the low Li$^+$ diffusion and electron transport.[4-6] Thus, it is necessary to develop new electrode materials for LIBs to meet the demands for high energy and power density, safety and long cycling

performance. Among the various electrode materials, TiO$_2$ has been considered as an electro-active material because of its high activity, low mass density, high abundance, nontoxicity and electrochemical and structural stability.[7-11] In addition, despite having a marginally high working potential, TiO$_2$ has received much attention as an anode material due to its avoidance of the formation of the solid electrolyte interfacial (SEI) layers for better safety.[11-13]

The Li storage performance of TiO$_2$ strongly depends on its crystallinity, particle size, morphology and porous structure, which can control the lithium ions diffusion and electrons transport.[9-12, 14-17] In particular, porous hollow TiO$_2$ spheres offer more sites for Li$^+$ insertion due to high specific surface area, accommodate volume change during charge/discharge cycles and reduce the diffusion pathway for Li$^+$ and electron transport to enhance the LIB performance.[18-21] Recently, significant efforts have been dedicated to synthesize hollow or core-shell or yolk-shell TiO$_2$ porous structures through template-free strategy.[22-31] Generally, this strategy involves aggregation of nanoparticles to a spherical morphology to reduce the high surface energy of the newly formed small crystallites followed by dissolution of the crystallites inside the sphere and recrystallization at the surface of the sphere, thus giving rise to special hollow or core-shell or yolk-shell structures.

Compared to the traditional hollow structures, the yolk-shell, a new class of core-shell structure with a distinctive core-void-shell configuration have certain advantages for LIBs. Indeed, yolk-shell configuration may improve structural stability, volumetric specific

a. Laboratory of Living Materials at the State Key Laboratory of Advanced Technology for Materials Synthesis and Processing, Wuhan University of Technology, 122 Luoshi Road, 430070 Wuhan, Hubei, China; Email: yu.li@whut.edu.cn and baoliansu@whut.edu.cn
b. Center of Electron Microscopy and State Key Laboratory of Silicon Materials, Department of Materials Science and Engineering, Zhejiang University, 310027 Hangzhou, Zhejiang, China.
c. Cambridge Graphene Centre, University of Cambridge, Cambridge, CB3 0FA, United Kingdom.
d. Laboratory of Inorganic Materials Chemistry (CMI), University of Namur, 61 rue de Bruxelles, B-5000 Namur, Belgium; E-mail: bao-lian.su@unamur.be
e. Department of Chemistry and Clare Hall, University of Cambridge, Cambridge, CB2 1EW, United Kingdom; E-mail: bls26@cam.ac.uk

Nanoscale Accepted Manuscript

capacity and energy density, enabling the TiO$_2$ anode material with superior lithium storage performance.[28, 32-34] Yang *et al.* employed a strategy of combining template assisted growth with solvothermal alcoholysis to synthesize core-void-shell anatase TiO$_2$ nanoparticle aggregates with 177 mA h g^{-1} reversible capacity after 50 discharge-charge cycles at 1 C.[34] Yoon *et al.* synthesized pseudo-yolk-shell mesoporous TiO$_2$ spheres by a hydrothermal reaction without surfactant, which exhibited a similar capacity of 180 mA h g^{-1} for 10 cycles at 1 C.[28] However, both the above TiO$_2$ yolk-shell structures demonstrated short cycle numbers at high current rates. This is due to the non-uniform size and voids in the core-void-shell structure, poor monodispersity and the fragile shell constructed by aggregated nanoparticles, which cannot make full use of the merits of the yolk-shell structure. Synthesizing a yolk-shell TiO$_2$ structure with good monodispersity, uniform size, uniform and controlled void thickness and a porous and mechanically robust shell through a facile and effective process still remains a challenge.

Here, for the first time, we demonstrate a hierarchical nanosheet-constructed yolk-shell TiO$_2$ (NYTiO$_2$) porous microsphere architecture through a one-pot template-free solvothermal alcoholysis process for LIBs. This structure consists of a porous shell assembled by uniform, 2D TiO$_2$ nanosheets and a dense mesoporous core constructed by TiO$_2$ nanoparticles. Such NYTiO$_2$ microspheres provide stable and hierarchically porous framework, effective grain boundaries and short diffusion pathway for Li$^+$ and electron transport, strongly facilitating the Li$^+$ insertion capability. The sheet structure in the porous shell is favorable for Li$^+$ insertion. On the other hand, the voids between the nanoparticle-aggregared mesoporous core and the nanosheet-constructed porous shell can store the electrolyte and facilitate charge transfer across the electrode/electrolyte interface to enhance the Li$^+$ insertion capacity. More importantly, the voids in the yolk-shell porous structure can buffer the volume change during the lithium ion insertion/extraction, leading to a better cycle performance. Indeed, the hierarchical NYTiO$_2$ yolk-shell anode material demonstrate excellent reversible capacity of 225 mA h g^{-1} after 100 cycles at 1 C. In particular, at 10 C current density, the reversible capacity remains at 113 mA h g^{-1} after 100 cycles. SEM, TEM, HRTEM, STEM EELS and *ex-situ* XRD characterizations on the post-mortem electrode reveal formation of crystalline Li$_2$Ti$_2$O$_4$ nanoparticles upon discharge-charge process, contributing to the excellent electrochemical properties, especially for the increased capacity and extraordinarily high stability during the cycling process. Our work sheds light on the design and formation mechanism of novel yolk-shell metal oxides, in particular, as advanced anode materials for high performance LIBs.

2. Experimental Section

2.1 Materials

Titanium tetra isopropoxide (TTIP) was purchased from Aldrich. Anhydrous ethanol and isopropyl alcohol (IPA) were purchased from Sinopharm Chemical Reagent Ltd. Co. Tetraethylenepentamine (TEPA) was purchased from Aladdin. All the chemical reagents were used as received.

2.2 Synthesis of the hierarchical NYTiO$_2$ spheres

In a typical synthesis, 0.12 mL of TEPA was added into 84 mL of isopropyl alcohol. After the solution was magnetically stirred for 5 minutes, 3 mL of TTIP was added to the above solution. Then, the reaction solution was stirred for 30 minutes. Subsequently, the solution was transferred into a 150 mL Teflon-lined autoclave and kept at 200 °C for 24 h. After this solvothermal reaction, the reaction was allowed to naturally cool to room temperature. The pale yellow precipitate was collected via centrifugation, washed thoroughly with ethanol and dried at 60 °C. This product is designated as NYTiO$_2$. After calcination at 400 °C for 2 h with a heating rate of 2 °C min^{-1}, a white product was collected. This product is designated as NYTiO$_2$-400. In order to explore the role of TEPA, various contents (0, 0.01, 0.03, 0.06, 0.09, 0.12 and 0.15 mL) of TEPA were used in the solvothermal reaction system under the same process and reaction conditions, respectively.

2.3 Characterizations

X-ray diffraction (XRD) patterns were obtained on a Bruker D8 system with Cu Kα radiation (λ=0.15405 nm) with 40 mA and 40 kV. Scanning electron microscopy (SEM) observation was carried out using an S-4800 field emission SEM (FESEM, Hitachi, Japan). Transmission electron microcopy (TEM) and high resolution transmission electron microcopy (HRTEM) images of the samples were recorded on carbon coated copper grids by using a JEM-2100F microscope at an acceleration voltage of 200 kV. Nitrogen adsorption-desorption isotherms were obtained using a Tri Star surface area & porosity analyzer (Tri Star II 3020) at 77 K. The specific surface area was calculated by the Brunauer-Emmett-Teller (BET) method. The pore size distribution was calculated by the Barret-Joyner-Halenda (BJH) method. The high angle annular dark field (HAADF) scanning transmission electron microscopy (STEM) and STEM-EELS (electron energy loss spectroscopy) experiments were performed on the FEI Titan G2 80-200/ChemiSTEM microscope equipped with a probe aberration-corrector and a GIF Quantum energy filter. The microscope was operated at 200 kV acceleration voltage and 16 mrad convergence angle to get enough spatial resolution.

2.4 Electrochemical Characterization

Electrochemical experiments were performed with coin-type cells with pure lithium metal as both the counter electrode and the reference electrode at room temperature. The working electrode consisted of active material (NYTiO$_2$-400), a conductive agent (carbon black, super-P), and a polymer binder (poly(vinylidene difluoride), PVDF) in a 70:20:10 weight ratio. After these materials had been thoroughly mixed in an N-methyl-2-pyrrolidone (NMP) solution, the prepared slurry was coated on Cu foil. The coated electrode was dried at 120 °C in a vacuum oven for 12 h. Circular disk electrodes were punched from the foil and a lithium metal foil was used as the counter electrode. The electrolyte used was 1.0 M LiPF$_6$ in a 50:50 (w/w) mixture of ethylene carbonate and diethyl carbonate. Cell assembly was carried out in an argon-filled glove box. Cyclic voltammetry (1-3V) was performed using an electrochemical workstation (CHI 660C). The discharge-charge tests were performed using a battery tester (LAND) with a voltage window of 1-3 V at various current densities.

3. Results and discussions

The nanosheet-constructed yolk-shell TiO$_2$ porous spheres are prepared through a one-pot template-free process on the basis of an effective reaction system. Isopropyl alcohol (IPA) is selected as the solvothermal solvent and titanium tetra isopropoxide (TTIP) as the TiO$_2$ source. Under our well controlled reaction system, IPA can release a defined amount of water from its etherification, enough for the hydrolysis of TTIP. This process can not only avoid the fast hydrolysis of TTIP inducing quick precipitation of large, radomly despersed and sized TiO$_2$ particles due to its high reactivity but also allow control in the formation of uniform spherical structure (**Scheme 1A**). Another key point is the use of tetraethylenepentamine (TEPA) as a suitable structure directing reagent for nanosheet formation. Without adding TEPA, only irregular TiO$_2$ microspheres are formed (**Fig. S1**). TEPA is a linear amine-hydrocarbon molecule that contains three secondary amines and two primary amines, one at each end and is widely used to modify the surface of SiO$_2$ and TiO$_2$ for CO$_2$ capture due to ist easy formation of hydrogen bonding with the silicon alkoxides and titanium alkoxides.[35-38] Under the directing effect of TEPA, the nanosheets are formed according to the illustration shown in Scheme 1B. The product obtained with 0.01 mL TEPA in our reaction system displays the nanosheet structure (Scheme 1B inset), indicating the feasibility of nanosheet synthesis strategy. By adjusting the parameters in the reaction system, such as reaction temperature, content of TEPA and reaction time, the nanosheets formed in Scheme B can be self-assembled around the spherical core formed in Scheme A. This leads to the formation of hierarchical nanosheet-constructed yolk-shell TiO$_2$ structure in this facile one-pot template-free solvothermal alcoholysis process summarized in Scheme 1C.

The reaction temperature was investigated at 160, 180 and 200 °C. We find that the hierarchical NYTiO$_2$ structure can only be formed at 200 °C (**Fig. S2**), indicating that only 200 °C can provide enough energy for the TEPA to direct the nanosheet formation and to self-assemble to yolk-shell structure. As the flash point of TEPA is around 164 °C, higher temperatures were not investigated considering safety in this experiment.

It is also worth mentioning that the appropriate content of TEPA is critical for the formation of hierarchical NYTiO$_2$ spheres. Our results show that 0.12 mL of TEPA is the optimum concentration. The importance of TEPA concentration on the formation of yolk-shell structure is shown in **Fig. S3**. SEM images corresponding to the TEPA concentration demonstrate that only the appropriate TEPA content can lead to the formation of yolk-shell structure with the nanosheet-constructed shell.

XRD, SEM and TEM are then used to characterize the structure and morphology of the as-prepared NYTiO$_2$ sample with 0.12 mL TEPA at 200 °C. **Fig. 1a** displays an intense reflection of 2θ = 8.5°, corresponding to the lamellar structure with a layer spacing of ~10.4 Å. In addition, several reflections in the region of 2θ = 20~80° are also observed, which can be indexed to the anatase phase (JCPDS No. 071-1167). Considering the SEM observations, these anatase reflections are expected to be from the nanoparticle-constructed inner core (Fig. S2c, S3e and Fig. 1c, 1d) and the lamellar structure from the nanosheet-constructed porous shell. All the anatase reflections have a large half-peak width, indicating low crystallinity.
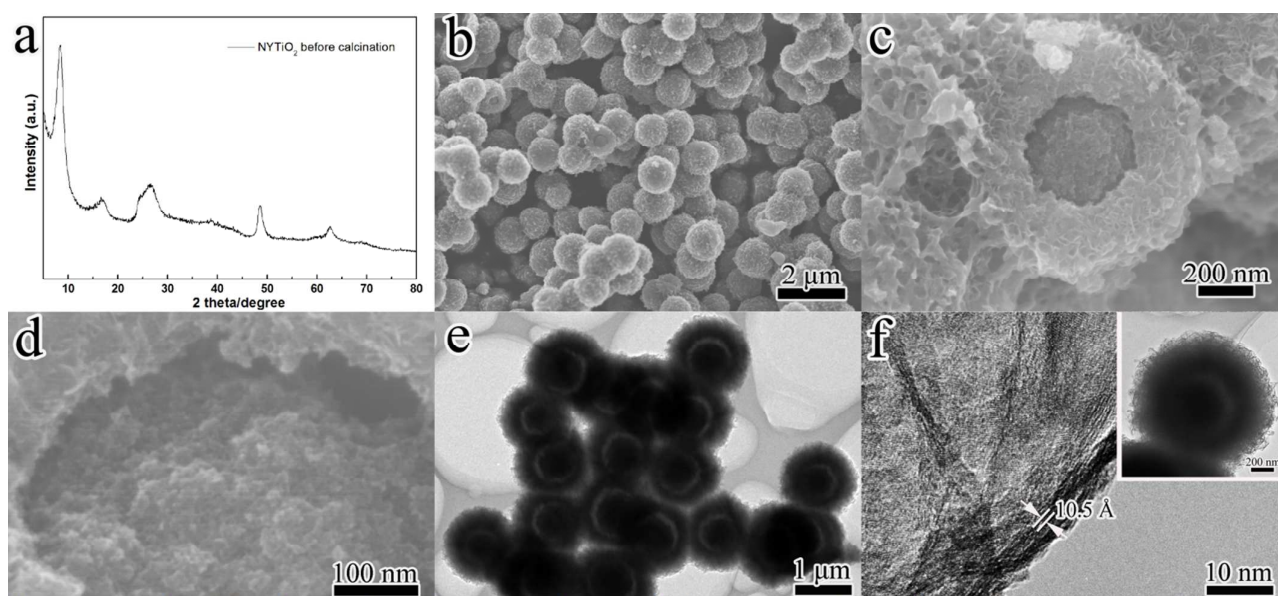
Fig. 1. Structure and morphology characterizations of the NYTiO$_2$ sample. (a) XRD, (b)-(d) SEM, (e) TEM of the microspheres and (f) HRTEM of 2D-nanosheets forming the shell. The inset in (f) is the low magnification TEM image of the corresponding microsphere.
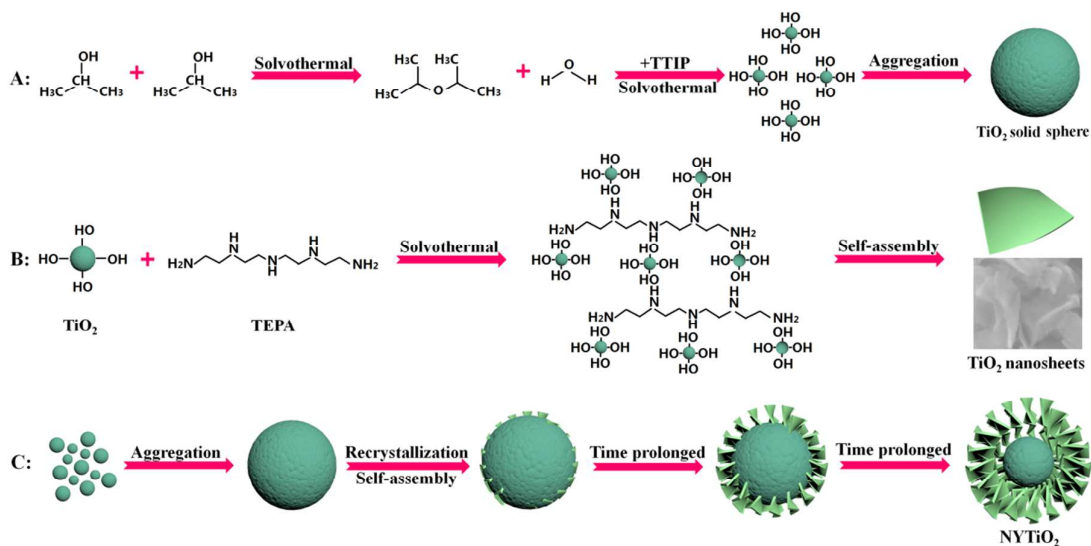
Scheme 1. (A) Formation of solid microspheres under solvothermal reaction without TEPA, (B) Formation of nanosheets under solvothermal reaction with a low concentration of TEPA, (C) Schematic growth diagram of hierarchical NYTiO$_2$.

SEM observations show that the as-prepared NYTiO$_2$ are uniformly monodispersed microspheres with an average size of ~1 µm (Fig. 1b). A broken microsphere shows the yolk-shell structure with a wall thickness of ~225 nm (Fig. 1c). The shell is formed by the assembly of nanosheets. The yolk or inner core is an aggregation of small nanoparticles (Fig. 1d and Fig. S4). The yolk-shell structure is further revealed by the TEM image as shown in Fig. 1e. It shows that all the cores are completely encapsulated by the shells with uniform and thin voids between the core and the shell, revealing a uniform core-void-shell structure (Fig. S5a). The void between the core and the shell is ~80 nm. The core has an average diameter of ~400 nm while the shell has a thickness of ~220 nm, which is consistent with the TEM observations (Fig. 1e). The shell is constructed by many lamellar nanosheets with 1~2 nm thickness (Fig. 1f and the inset), which grow radially outside with 10.5 Å interlayer spacing, in good agreement with the XRD analysis.

Such yolk-shell TiO$_2$ porous microspheres with nanosheet-constructed shell and nanoparticle-aggregated core and their formation mechanism has never been reported in the literature. A detailed time dependent evolution process is used to investigate the formation mechanism of these hierarchical NYTiO$_2$ structure. Fig. 2 shows the SEM images of the products obtained at different growth stages. After 1.5 h reaction, some irregular particles accompanying with the size of 100~200 nm spheres appear in the product (Fig. 2a). These are likely due to the aggregation of the crystallites formed from the TTIP hydrolysis as they minimize their surface energy. When the reaction time is prolonged to 3 h (Fig. 2b), some surface smooth TiO$_2$ spheres with an average size of ~600 nm are formed due to the continuous agglomeration of the irregular TiO$_2$ nanoparticles to reduce the surface energy. With a longer solvothermal reaction time of 6 h, the diameter of the smooth TiO$_2$ spheres grows to ~800 nm (Fig. 2c), indicating further aggregation of the irregular TiO$_2$ nanoparticles. When the reaction time is prolonged to 9 h, a ~1.1 µm yolk-shell structure consisting of a spherical core and a 50 nm thick nanosheet-constructed shell is formed (Fig. 2d and 2e). With a longer reaction time, the diameter of the whole yolk-shell structure remains virtually unchanged (Fig. 2f). However, the size of the core gradually decreases while the shell thickens. Indeed for a 24 h reaction time, the core is decreased to ~400 nm and the shell is increased to ~220 nm (Fig. 2g and 2h), leading to void formation between the nanoparticle-aggregated core and nanosheet-constructed shell.
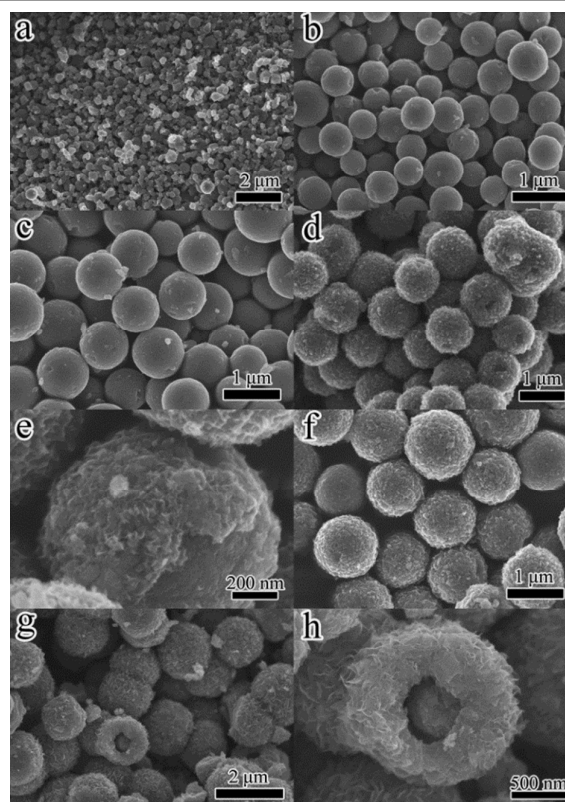
Fig. 2. The morphology evolution of the hierarchical NYTiO$_2$ structure. (a) 1.5 h, (b) 3 h, (c) 6 h, (d)-(e) 9 h, (f) 12 h, (g)-(h) 24 h.

On the basis of the above observation and analysis, a possible formation mechanism of the hierarchical NYTiO$_2$ spheres is proposed in Scheme 1C. At the beginning of reaction, the freshly formed tiny TiO$_2$ crystallites spontaneously aggregate to form numerous poorly crystallized TiO$_2$ solid spheres with smooth surface to reduce high surface energy.[39] Compared to the nanoparticles at the outer surfaces, the nanoparticles located in the inner cores have high surface energy and tend to dissolve and recrystallize under the high temperature.[40] In addition, hydrogen-bonds, such as N-H and O-H bonds constructed between IPA (containing O and H atoms)/TEPA (containing N and H atoms) and the TiO$_2$ nanoparticles (with a lot of hydroxyl on the surface of the TiO$_2$ particles), can increase the interconnection between the formed nanoparticles.[29] In strong polar solvents and high reaction temperature, the nanoparticles at the core are gradually dissolved

and recrystallized to the nanosheets directed by TEPA. At the beginning of the recrystallization process, the growth speed of the nanosheets is slow. There is no obvious void between the core and the shell (Fig. 2d). As the reaction progresses, the recrystallization speed of the nanosheets increases and becomes higher than the dissolution speed of the inner core. The void between the core and the shell appears and grows larger as the reaction proceeds. Finally, with 24 h reaction time, the hierarchical NYTiO$_2$ structure is obtained. It is also worth noting that at the content of TEPA from 0.01 mL to 0.09 mL, the amount of the products is low, indicating less recrystallization of the dissolved nanocrystallites. In particular, a low content of 0.01 mL TEPA, the small amount of formed nanosheets can not self-assemble to the spherical structure, resulting in appearance of only fragments of nanosheets (Fig. S3a).
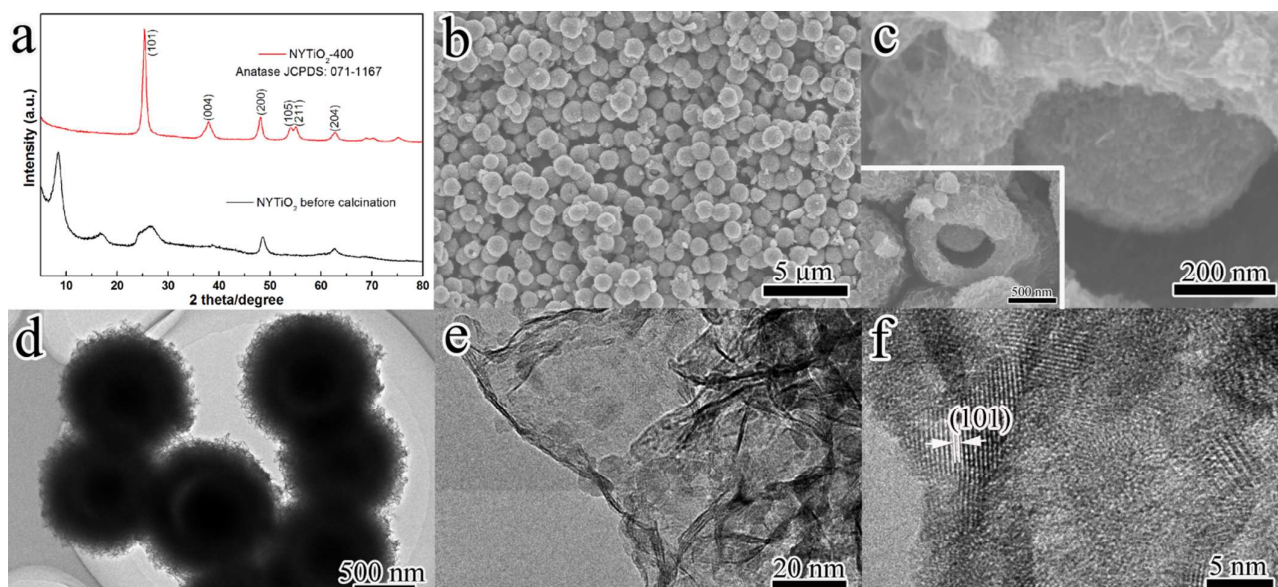
Fig. 3. Structure and morphology characterizations of the NYTiO$_2$-400 sample. (a) XRD, (b)-(c) SEM, (d)-(e)TEM and (f) HRTEM images. The inset in (c) is the low magnification SEM image of the corresponding yolk-shell sphere.

The as-prepared NYTiO$_2$ is then calcined at 400 °C (NYTiO$_2$-400) under air for 2 hours for further crystallization to desired anatase phase. Fig. 3a shows the XRD patterns of the NYTiO$_2$-400 sample. After calcination at 400 °C, the peak at 8.5° disappears, indicating the disappearance of the lamellar structure along with the recrystallization of the NYTiO$_2$ sample. All the peaks of the NYTiO$_2$-400 can be well indexed to the anatase phase (JCPDS No. 071-1167). Fig. 3b displays the well-kept spherical morphology after calcination. Fig. 3c and the inset show that the hierarchical NYTiO$_2$ structure with a nanosheet-constructed shell can be completely retained after the calcination. The core is still constructed by the self-assembled TiO$_2$ nanoparticles (Fig. S6). The TEM image in Fig. 3d exhibits a perspective view of the yolk-shell structure of the NYTiO$_2$-400. It also displays that the voids between the core and the shell are enlarged from ~80 nm for the as-prepared NYTiO$_2$ to ~120 nm for the NYTiO$_2$-400 (Fig. S5b). The enlarged void space between the core and shell is helpful for storing the electrolyte and facilitating charge transfer across the electrode/electrolyte interface and buffering the volume change during the Li$^+$

insertion/extraction, resulting in enhanced Li$^+$ insertion capacity and cycling performance. Fig. 3e displays the nanosheet structure of the shell, indicating the well-kept sheet structure. Compared with the as-prepared NYTiO$_2$, the nanosheets of the NYTiO$_2$-400 (Fig. 3f) demonstrate a much higher crystallinity, well consistent with the XRD result (Fig. 3a). The lattice spacing of 0.35 nm, corresponding to the (101) plane of anatase, can be observed in the nanosheet structure, confirming the transformation of the initial lamellar structure to anatase phase. The HRTEM image also demonstrates that there exist also some amorphous regions and pores in the nanosheets (Fig. 3f), which are very important to provide high surface area and more active sites for Li$^+$ insertion to promote the Li$^+$ storage.

The specific surface area and pore size distribution of the NYTiO$_2$-400 are characterized by N$_2$ adsorption-desorption (Fig. S7). The result exhibits a type-IV isotherm, indicating the presence of the mesoporous structure. The NYTiO$_2$-400 sample demonstrates a high specific surface area of 168 m^2 g^{-1} and an adsorption cumulative volume of 0.7 cm^3 g^{-1}. Very interestingly, dual pore sizes

of 15 nm and 3 nm are observed. Upon intensive SEM and TEM characterizations, we attribute the 15 nm pore to the outer porous shell formed by the assemblly of nanosheets and the 3 nm pore to the inner mesoporous core assembled by small nanoparticles. The bimodal pore distribution in the yolk-shell structure are helpful for Li^+ storage.

The principle reaction that governs the electrochemical processes in TiO_2/Li half-cell can be written as

$$xLi^+ + xe^- + TiO_2 \leftrightarrow Li_xTiO_2 \qquad (1),$$
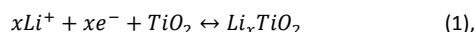
corresponding to the complete reduction of Ti^{4+} to Ti^{3+} and theoretical capacity of anatase TiO_2 at 335 mA h g^{-1}. However, the elastic interaction force between intercalated lithium ions and the formation of weak Ti-Ti interactions results in the lithium ions randomly distributing over half of the available interstitial octahedral sites. Therefore, from a practical point of view, the maximum reversible insertion level is limited to an insertion coefficient of 0.5 Li per formula unit of TiO_2, corresponding to the two equilibrium phases of the Li-poor $Li_{0.05}TiO_2$ and the Li-rich

$Li_{0.5}TiO_2$. The associated reversible capacity is then 168 mA h g^{-1}. Additional capacity (x>0.5) is generally related to the surface storage mechanisms, connected to pseudocapacities strictly depending on the porosity and the surface area.[41-43]

Fig. 4a displays the representative cyclic voltammograms (CVs) of the $NYTiO_2$-400 electrode at 0.5 mV s^{-1}. In the first cycle, two well-defined peaks can be observed at ~1.5 V (cathodic sweep) and ~2.2 V (anodic sweep) for the $NYTiO_2$-400 electrode. In the following few cycles, the cathodic peak is shifted to 1.65 V, while the anodic peak stays unchanged, suggesting a possible activating process. It is worth to note that there are weak scan peaks near ~1.45 V (cathodic sweep) and ~1.6 V (anodic sweep). These scan peaks may belong to the characteristic peaks of TiO_2(B) according to the previous reports.[44-46] As our $NYTiO_2$-400 is obtained by calcination of layered structure, we can not exclude the TiO_2(B) formation in the sample, although the peaks of TiO_2(B) have not been distinguished by XRD and HRTEM characterizations due to the very small amount in $NYTiO_2$-400. Further work should be carried out to clarify this.
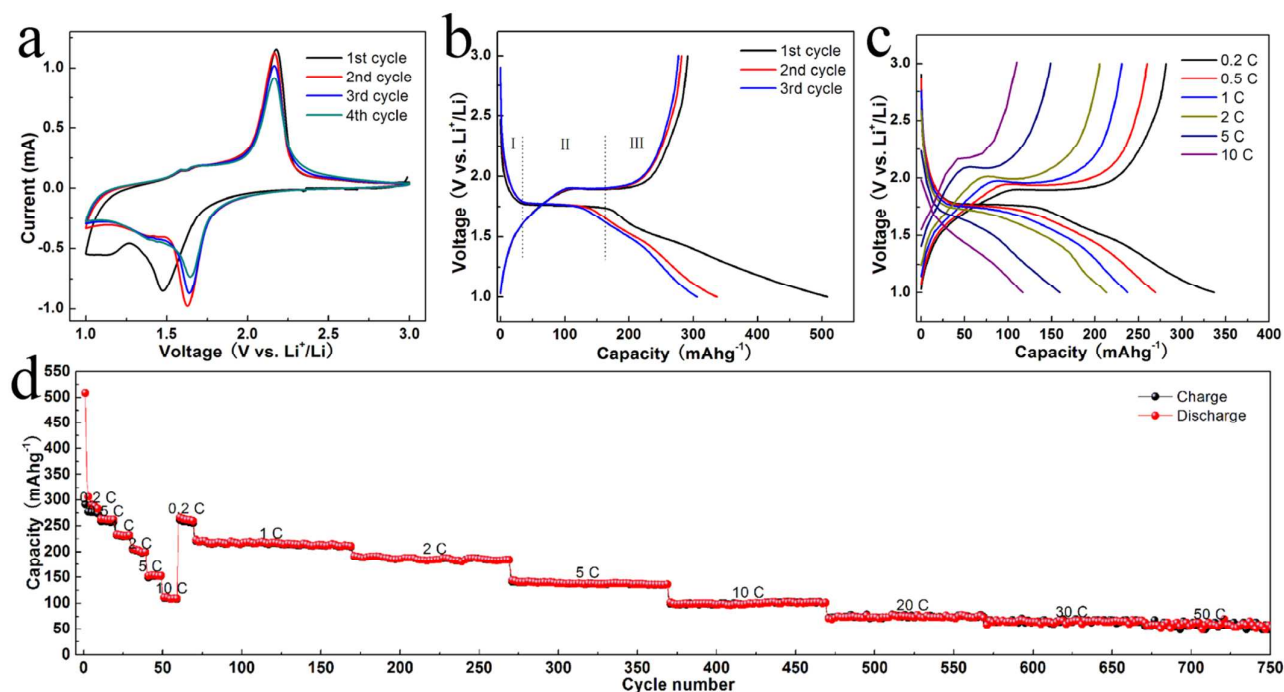
Fig. 4. The electrochemical properties of the $NYTiO_2$-400 anode material. (a) representative CVs at a scan rate of 0.5 mV s^{-1} for the first, second, third and fourth cycles; (b) discharge-charge profiles at a current of 0.2 C for the first, second and third cycles; (c) discharge-charge profiles and (d) cycle and rate performances at various discharge-charge rates. The dash lines indicate the different stages for the discharging process.

Fig. 4b depicts the discharge-charge profiles of the $NYTiO_2$-400 electrode for the first, second and third cycles at a current of 0.2 C (1 C = 168 mA g^{-1}). Two well-defined voltage plateaus appear at ~1.8 V and ~1.9 V during the discharge and charge processes, consistent with the CV analysis. The Li^+ insertion process can be divided into three stages (region I, II and III). For the first stage (region I) of the discharge curve in the first cycle, the potential drops from the open circuit value of ~2.9 V to a value of ~1.8 V with a Li^+ insertion capability of 34 mA h g^{-1}. This stage is often ascribed either to a pseudocapacitive-like surface effect[43] or to the formation of a solid solution of TiO_2 and $Li_\varepsilon TiO_2$.[42] The second stage

(region II) is the horizontal plateau region, which reflects the process of Li^+ insertion into the vacant sites of the TiO_2 crystal structure, with a Li^+ insertion capability of 135 mA h g^{-1}. The last stage (region III) is the gradual decay of the voltage after the plateau region, which reflects the insertion process of Li^+ into the surface layer of the anode material, with a Li^+ insertion capability of 340 mA h g^{-1}. The initial discharge capacity is 509 mA h g^{-1} with *ca.* 1.5 Li insertion and the subsequent charge capacity is 291 mA h g^{-1} with *ca.* 0.9 Li extraction, leading to a coulombic efficiency of 60%. The discharge and charge capacities in the second cycle are 337 and 282 mA h g^{-1}, respectively, leading to a high coulombic efficiency of

84%. The coulombic efficiency is increased further to 91% in the third discharge-charge cycle, indicating the fast balance of the lithium ions insertion and extraction in the subsequent discharge-charge processes owing to the hierarchically porous yolk-shell structure.

Fig. 4c displays the discharge-charge profiles of the NYTiO$_2$-400 electrode at various rates. The discharge capacities are 337, 269, 237, 213, 159 and 117 mA h g^{-1} at 0.2 C, 0.5 C, 1 C, 2 C, 5 C and 10 C, respectively. When the current rate is 0.2 C, the capacities of the first, second and third stages (region I, II and III) are 34, 101 and 202 mA h g^{-1}, respectively (Fig. S8). The capacities of the first, second and third stages (region I, II and III) are 34, 81 and 154 mA h g^{-1} at 0.5 C, 34, 44 and 159 mA h g^{-1} at 1 C and 34, 29 and 150 mA h g^{-1} at 2 C, respectively. These results clearly show that the decreased discharge capacities from 0.5 C to 2 C mainly correspond to the second stage (the voltage plateau stage). The higher kinetic efficiency of Li$^+$ insertion to the additional surface (the third stage) than that to the crystal structure (the second stage) should be the primary reason for this phenomenon, likely due to the dual porosities in the yolk-shell structure.

Fig. 4d shows the cycle performances of the NYTiO$_2$-400 electrode at various discharge-charge rates. When discharged at 0.2 C, the NYTiO$_2$-400 has an initial discharge capacity of 509 mA h g^{-1} and a subsequent charge capacity of 291 mA h g^{-1}. When discharged at 0.2 C for 10 cycles, the NYTiO$_2$-400 anode has a discharge capacity of 283 mA h g^{-1} and a subsequent charge capacity of 273 mA h g^{-1}, leading to a high coulombic efficiency of 97%. While the current densities are increased to 0.5 C, 1 C, 2 C, 5 C and 10 C, the discharge capacities are decreased to 269, 237, 213, 159 and 117 mA h g^{-1}, respectively. As the current rate is put back to 0.2 C, the discharge capacity of the NYTiO$_2$-400 is increased to 263 mA h g^{-1}. The rate performance is further tested on the same unit. When the NYTiO$_2$-400 electrode is discharged for more than 100 cycles at 1C, a reversible capacity of 225 mA h g^{-1} is retained, leading to a lithium insertion coefficient of 0.67. A 185 mA h g^{-1} reversible capacity is retained after 100 cycles at 2 C. Furthermore, when the current density is increased to 5 C, 10 C, 20 C and 30 C, the reversible capacity is decreased to 137, 113, 76 and 67 mA h g^{-1} after 100 cycles, respectively. Even at 50 C for >70 cycles, the reversible capacity remains at 58 mA h g^{-1}. The values in this work are among the best values reported for TiO$_2$ systems.[44-52] We attribute such high electrochemical performance to the hierarchically porous yolk-shell structure with outer porous nanosheets shell and inner mesoporous core.

To further understand the lithium storage property and structural stability of the NYTiO$_2$-400 anode material, post-mortem studies after 100 discharge-charge cycles at 1 C are carried out through SEM, TEM and STEM-EELS observations. For the post-mortem studies, the NYTiO$_2$-400 anode material after 100 cycles at 1C is removed from the unit and immersed in the acetonitrile solution for a week to wash off the electrolyte. Fig. 5a-c show that all the hierarchical yolk-shell structures are retained after the electrochemical reaction, indicating the structural and electrochemical stabilities of the NYTiO$_2$-400 material. This leads to the excellent capacity retention and superior rate performance. Interestingly, after the lithium insertion, many small nanoparticles with 5~10 nm diameter can be observed. These are randomly but uniformly distributed on the nanosheets (Fig. 5d). The corresponding SAED patterns taken from one NYTiO$_2$-400 sphere after 100 cycles are shown in Fig. 5e. The electron diffraction rings can be indexed to be anatase and cubic Li$_2$Ti$_2$O$_4$ (space group: *F3m3*, lattice constants: a = b = c = 8.375 Å), respectively. From the HRTEM image (Fig. 5f and the inset), the lattice spacing of the particle is measured to be 2.09 Å, corresponding to the (400) crystal plane of Li$_2$Ti$_2$O$_4$, confirming the formation of Li$_2$Ti$_2$O$_4$ nanocrystallites.[50, 51, 53-55] STEM-EELS element mapping is next utilized to study the spatial elemental distribution after the phase transition. Fig. 6a-e display the elemental distribution images of the lithiated NYTiO$_2$-400 anode material. The EELS elemental mapping is conducted on an area as shown in Fig. 6a. Fig. 6c and 6d indicates that the distribution of O and Ti elements is uniform. However, the Li elements are non-uniformly distributed in the selected area (Fig. 6b). To better understand the chemical distribution of Li, O and Ti elements, the three elemental maps are superimposed in Fig. 6e. It shows that the Li element is mainly focused in ~7 nm islands, indicating the existence of the Li$_2$Ti$_2$O$_4$ nanocrystallites. This is consistent with the TEM result in Fig. 5d. Therefore, the Reaction 1 can be modified to contain the new Li$_2$Ti$_2$O$_4$ phase according to

$$2(1-x)Li^+ + 2(1-x)e^- + 2Li_xTiO_2 \leftrightarrow Li_2Ti_2O_4 \qquad (2).$$
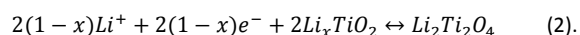
It can be inferred from the above TEM results that the continuous lithium insertion as Li$_x$TiO$_2$ will lead to an atomic rearrangement on the nanosheet-constructed shell structure to form the new cubic crystals of Li$_2$Ti$_2$O$_4$ with one Li inserted per formula unit of TiO$_2$. Hence, this crystalline Li$_2$Ti$_2$O$_4$ islands can further facilitate the Li$^+$ insertion capability and thus enhance the Li$^+$ storage capacity by providing additional surface capacity at the third stage, resulting in an excellent electrochemical performance.
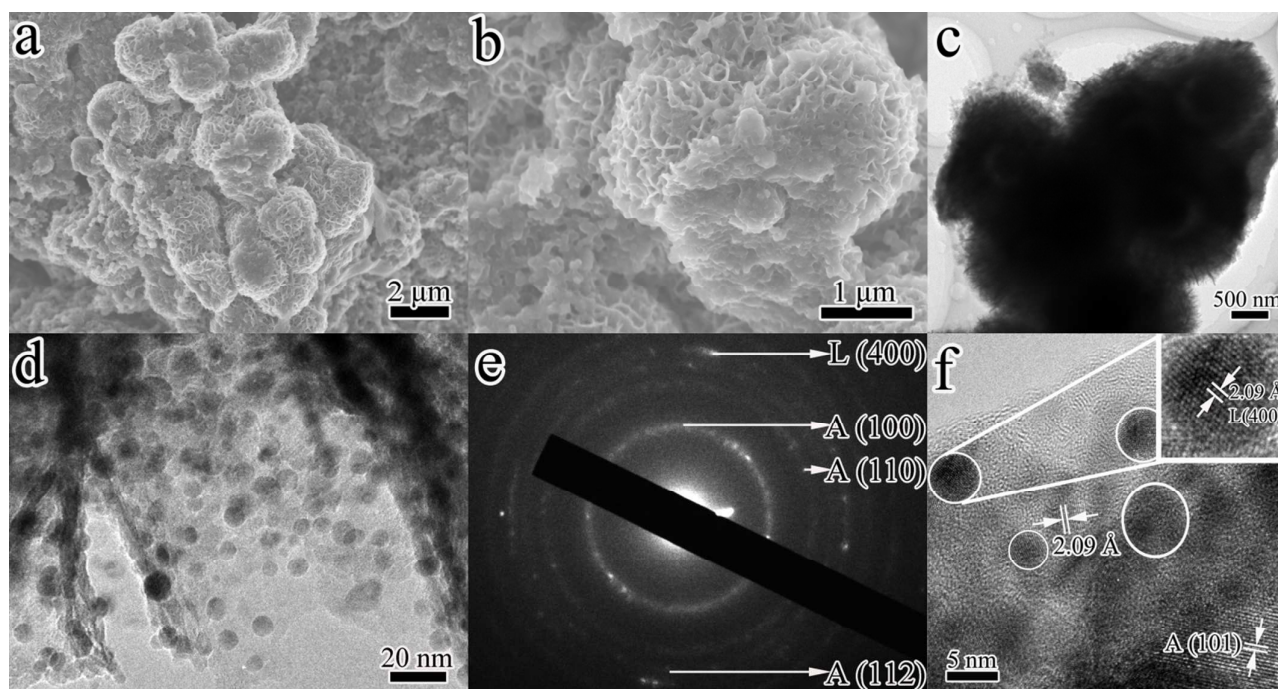
Fig. 5. Post-mortem studies of the NYTiO$_2$-400 anode material on the state of discharge after 100 discharge-charge cycles at 1 C. (a)-(b) SEM images, (c)-(d) TEM images, (e) SAED pattern, (f) HRTEM image, and inset of Fig. 5f: HRTEM image of one Li$_2$Ti$_2$O$_4$ nanoparticle. A and L in (e) represent the anatase and Li$_2$Ti$_2$O$_4$ phases, respectively.

Next *ex-situ* XRD technique is utilized to detect the crystalline structure of the NYTiO$_2$-400 anode material on the state of discharge. The lithiated NYTiO$_2$ anode material was removed from the cycled half-cell for *ex-situ* XRD study. Fig. S9 shows the XRD patterns of the NYTiO$_2$-400 sample and discharged (to 1 V) NYTiO$_2$-400 anode material, respectively. Compared with the as-prepared NYTiO$_2$-400, the diffraction peaks of the discharged NYTiO$_2$-400 from the initial anatase phases are weaken, especially the (101) and (004) planes, indicating the Li$^+$ insertion during the discharge process. The appearance of diffraction peak at 39.6° and the broadness of diffraction peaks at 38.0° indicate the formation of a Li$_2$Ti$_2$O$_4$ phase, in agreement with the previous study.[10] The continued intercalation of Li ions leads to the formation of Li$_2$Ti$_2$O$_4$ nanocrystallites.
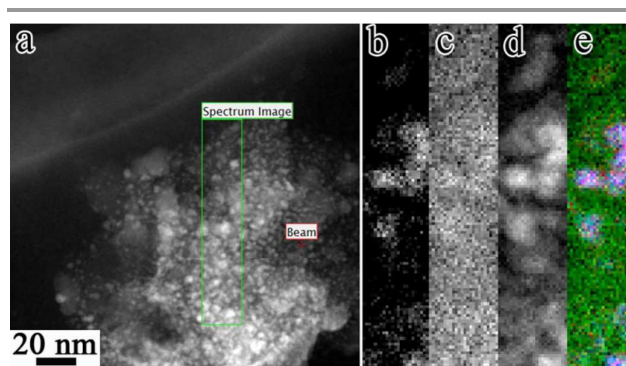
Fig. 6. (a) HAADF-STEM and (b)-(e) STEM EELS mapping images: (b) Li; (c) O; (d) Ti; (e) composite color map (Red: Li; Blue: Ti; Green: O).
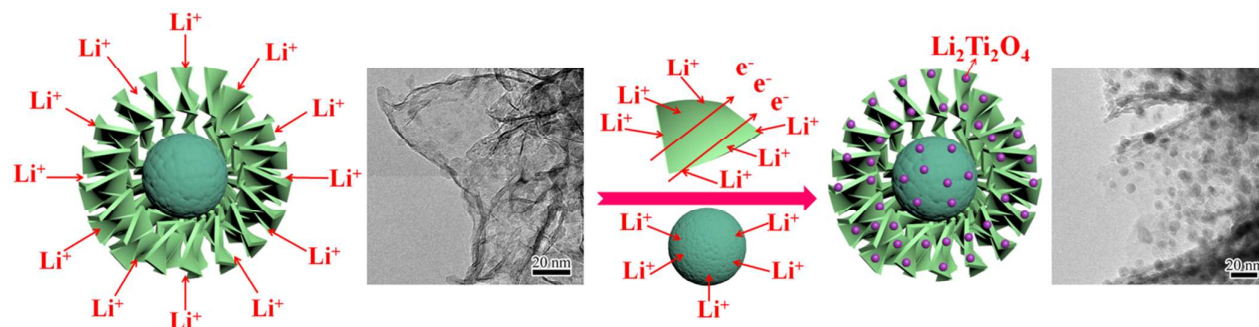
Scheme 2. The Li$^+$ insertion process of the hierarchical NYTiO$_2$ anode material and the formation of the Li$_2$Ti$_2$O$_4$ nanocrystallites.

On the basis of the results and post-mortem characterizations, a possible Li$^+$ insertion mechanism into the hierarchical NYTiO$_2$ structure is proposed in Scheme 2. The Li$^+$ can quickly intercalate into the nanosheet-constructed TiO$_2$ porous shell, leading to the

formation of Li_xTiO_2 matrix, indicating the excellent Li^+ insertion capability. Then, with further Li^+ insertion into the Li_xTiO_2 matrix, a new $Li_2Ti_2O_4$ crystalline structure is formed. The new $Li_2Ti_2O_4$ islands are homogenously distributed on to the porous nanosheets. Although the core has not been studied for the presence of $Li_2Ti_2O_4$ nanocrystallites, we believe that they are also formed in the core during the discharge-charge process. The $Li_2Ti_2O_4$ crystals further facilitate the Li^+ insertion capability and enhance the overall Li^+ storage capacity by providing additional surface capacity at the third stage during the discharge-charge process. The synergy of the hierarchically porous $NYTiO_2$ yolk-shell structure with outer nanosheet-constructed porous shell and inner nanoparticles-aggregated mesoporous core and the formed $Li_2Ti_2O_4$ nanocrystallites ensure the high reversible capacity, excellent rate capability and outstanding cycle performance.

4. Conclusions

A one-pot template-free solvothermal alcoholysis process has been employed for structural and morphological engineering of TiO_2 and gave rise to the hierarchical nanosheet-constructed yolk-shell TiO_2 microspheres. The TEPA plays a very important role in the formation of TiO_2 nanosheet and further directs nanosheet self-assembly during the recrystallization process to form the hierarchically porous $NYTiO_2$ microspheres. The resulting hierarchical anatase $NYTiO_2$ porous spheres demonstrate a high specific surface area of 168 $m^2\ g^{-1}$, a high cumulative volume of 0.7 $cm^3\ g^{-1}$ and bimodal pore distribution of 15 nm and 3 nm. Thanks to the uniform yolk-shell TiO_2 structure with outer 2D nanosheet-constrcuted porous shell and inner nanoparticles-aggregated mesopores core structure with good mechanical stability, the anatase $NYTiO_2$ anode material can provide continuous and short transport pathway for Li^+ and electron and facilitate the Li^+ insertion. Through the porous shell structure, Li^+ can continuously intercalate into the TiO_2 to form a Li_xTiO_2 matrix. A new $Li_2Ti_2O_4$ crystalline grain with 5~10 nm size further facilitates the surface capability, enhancing the Li^+ storage capacity. Our anatase $NYTiO_2$ porous spheres demonstrate excellent specific capability with high capacity, good cycle performance and superior rate capacity due to the hierarchical yolk-shell structure and the formed $Li_2Ti_2O_4$ crystalline islands. The hierarchically porous spheres may also be employed in other applications, such as drug delivery, photocatalytic water splitting, dye-sensitized solar cells and gas sensors. In addition, our synthesis strategy on the yolk-shell microspheres with dual porosities should shed new light on designing novel core-shell porous structures for high performance LIBs.

Acknowledgements

Notes and references

1. J. M. Tarascon and M. Armand, *Nature*, 2001, **414**, 359-367.
2. H. g. Zhang, X. d. Yu and P. V. Braun, *Nat. Nanotechnol.*, 2011, **6**, 277-281.
3. P. G. Bruce, B. Scrosati and J. M. Tarascon, *Angew. Chem. Int. Ed.*, 2008, **47**, 2930-2946.
4. A. S. Aricò, P. Bruce, B. Scrosati, J. M. Tarascon and W. Van Schalkwijk, *Nat. Mater.* 2005, **4**, 366-377.
5. J. Y. Shin, J. H. Joo, D. Samuelis and J. Maier, *Chem. Mater.*, 2012, **24**, 543-551.
6. S. Z. Huang, J. Jin, Y. Cai, Y. Li, H. Y. Tan, H. E. Wang, G. Van Tendeloo and B. L. Su, *Nanoscale*, 2014, **6**, 6819-6827.
7. J. Ye, W. Liu, J. Cai, S. Chen, X. Zhao, H. Zhou and L. Qi, *J. Am. Chem. Soc.*, 2010, **133**, 933-940.
8. B. Zhao and Z. Shao, *J. Phys. Chem. C*, 2012, **116**, 17440-17447.
9. M. Reddy, G. Subba Rao and B. Chowdari, *Chem. Rev.*, 2013, **113**, 5364-5457.
10. K. Shen, H. Chen, F. Klaver, F. M. Mulder and M. Wagemaker, *Chem. Mater.*, 2014, **26**, 1608-1615.
11. Y. Li, Z. Y. Fu and B. L. Su, *Adv. Funct. Mater.*, 2012, **22**, 4634-4667.
12. M. Wagemaker, G. J. Kearley, A. A. van Well, H. Mutka and F. M. Mulder, *J. Am. Chem. Soc.*, 2003, **125**, 840-848.
13. H. E. Wang, J. Jin, Y. Cai, J. M. Xu, D. S. Chen, X. F. Zheng, Z. Deng, Y. Li, I. Bello and B. L. Su, *J. Colloid Interface Sci.*, 2014, **417**, 144-151.
14. J. Jin, S. Z. Huang, J. Liu, Y. Li, D. S. Chen, H. E. Wang, Y. Yu, L. H. Chen and B. L. Su, *J. Mater. Chem. A*, 2014, **2**, 9699-9708.
15. T. Lan, Y. Liu, J. Dou, Z. Hong and M. Wei, *J. Mater. Chem. A*, 2014, **2**, 1102-1106.
16. F. F. Cao, X. L. Wu, S. Xin, Y. G. Guo and L. J. Wan, *J. Phys. Chem. C*, 2010, **114**, 10308-10313.
17. Y. Qiu, K. Yan, S. Yang, L. Jin, H. Deng and W. Li, *ACS nano*, 2010, **4**, 6515-6526.
18. H. G. Jung, C. S. Yoon, J. Prakash and Y. K. Sun, *J. Phys. Chem. C*, 2009, **113**, 21258-21263.
19. J. Wang, Y. Zhou, Y. Hu, R. O'Hayre and Z. Shao, *J. Phys. Chem. C*, 2011, **115**, 2529-2536.
20. S. Ding, J. S. Chen, Z. Wang, Y. L. Cheah, S. Madhavi, X. Hu and X. W. Lou, *J. Mater. Chem.*, 2011, **21**, 1677-1680.
21. J. Wang, Y. Bai, M. Wu, J. Yin and W. Zhang, *J. Power Sources*, 2009, **191**, 614-618.

22. Y. Yin, R. M. Rioux, C. K. Erdonmez, S. Hughes, G. A. Somorjai and A. P. Alivisatos, *Science*, 2004, **304**, 711-714.

23. H. C. Zeng, *J. Mater. Chem.*, 2011, **21**, 7511-7526.

24. L. Cao, D. Chen and R. A. Caruso, *Angew. Chem. Int. Ed.*, 2013, **52**, 10986-10991.

25. J. H. Pan, X. Zhang, A. J. Du, D. D. Sun and J. O. Leckie, *J. Am. Chem. Soc.*, 2008, **130**, 11256-11257.

26. M. Xu, P. Ruan, H. Xie, A. Yu and X. Zhou, *ACS Sustainable Chem. Eng.*, 2014, **2**, 621-628.

27. H. Li, Z. Bian, J. Zhu, D. Zhang, G. Li, Y. Huo, H. Li and Y. Lu, *J. Am. Chem. Soc.*, 2007, **129**, 8406-8407.

28. S. Yoon and A. Manthiram, *J. Phys. Chem. C*, 2011, **115**, 9410-9416.

29. D. Li, Q. Qin, X. C. Duan, J. Q. Yang, W. Guo and W. J. Zheng, *ACS Appl. Mater. Interfaces*, 2013, **5**, 9095-9100.

30. Z. Bian, J. Zhu, J. Wang, S. Xiao, C. Nuckolls and H. Li, *J. Am. Chem. Soc.*, 2012, **134**, 2325-2331.

31. N. Sutradhar, S. K. Pahari, M. Jayachandran, A. M. Stephan, J. Nair, B. Subramanian, H. C. Bajaj, H. M. Mody and A. B. Panda, *J. Mater. Chem. A*, 2013, **1**, 9122-9131.

32. G. Liu, Z. Su, S. Sarfraz, K. Xi and C. Lai, *Mater. Lett.*, 2012, **84**, 143-146.

33. W. Wang, Q. Sa, J. Chen, Y. Wang, H. Jung and Y. Yin, *ACS Appl. Mater. Interfaces*, 2013, **5**, 6478-6483.

34. H. Guo, D. Tian, L. Liu, Y. Wang, Y. Guo and X. Yang, *J. Solid State Chem.*, 2013, **201**, 137-143.

35. S. H. Liu, W. C. Hsiao and W. H. Sie, *Adsorption*, 2012, **18**, 431-437.

36. E. Silva Mojica, University of Akron, 2011.

37. Q. Ye, J. Jiang, C. Wang, Y. Liu, H. Pan and Y. Shi, *Energy & Fuels*, 2012, **26**, 2497-2504.

38. Y. Liu, J. Shi, J. Chen, Q. Ye, H. Pan, Z. Shao and Y. Shi, *Microporous Mesoporous Mater.*, 2010, **134**, 16-21.

39. R. L. Penn and J. F. Banfield, *Science*, 1998, **281**, 969-971.

40. Z. Q. Sun, J. H. Kim, Y. Zhao, F. Bijarbooneh, V. Malgras, Y. m. Lee, Y. M. Kang and S. X. Dou, *J. Am. Chem. Soc.*, 2011, **133**, 19314-19317.

41. M. Wagemaker, W. J. Borghols and F. M. Mulder, *J. Am. Chem. Soc.*, 2007, **129**, 4323-4327.

42. G. Sudant, E. Baudrin, D. Larcher and J. M. Tarascon, *J. Mater. Chem.*, 2005, **15**, 1263-1269.

43. C. Jiang, M. Wei, Z. Qi, T. Kudo, I. Honma and H. Zhou, *J. Power Sources*, 2007, **166**, 239-243.

44. M. Zukalova, M. Kalbac, L. Kavan, I. Exnar and M. Graetzel, *Chem. Mater.*, 2005, **17**, 1248-1255.

45. Y. Tang, Y. Zhang, J. Deng, J. Wei, H. L. Tam, B. K. Chandran, Z. Dong, Z. Chen and X. Chen, *Adv. Mater.*, 2014, **26**, 6111-6118.

46. Y. Tang, Y. Zhang, J. Deng, D. Qi, W. R. Leow, J. Wei, S. Yin, Z. Dong, R. Yazami, Z. Chen and X. Chen, *Angew. Chem. Int. Ed.*, 2014, **53**, 1-6.

47. Z. Liu, J. Liu, J. Liu, L. Wang, G. Zhang and X. Sun, *PCCP*, 2014, **16**, 8808-8811.

48. H. E. Wang, H. Cheng, C. Liu, X. Chen, Q. Jiang, Z. Lu, Y. Y. Li, C. Chung, W. Zhang and J. A. Zapien, *J. Power Sources*, 2011, **196**, 6394-6399.

49. L. H. Nguyen, V. Aravindan, S. A. Kulkarni, F. Yanan, R. R. Prabhakar, S. K. Batabyal and S. Madhavi, *ChemElectroChem*, 2014, **1**, 539-543.

50. X. Jiang, X. Yang, Y. Zhu, H. Jiang, Y. Yao, P. Zhao and C. Li, *J. Mater. Chem. A*, 2014, **2**, 11124-11133.

51. J. X. Qiu, S. Li, E. Gray, H. W. Liu, Q. F. Gu, C. F. Sun, C. Lai, H. J. Zhao and S. Q. Zhang, *J. Phys. Chem. C*, 2014, **118**, 8824-8830.

52. R. W. Mo, Z. Y. Lei, K. N. Sun and D. Rooney, *Adv. Mater.*, 2014, **26**, 2084-2088.

53. V. Gentili, S. Brutti, L. Hardwick, A. Armstrong, S. Panero and P. Bruce, *Chem. Mater.*, 2012, **24**, 4468-4476.

54. Q. Gao, M. Gu, A. Nie, F. Mashayek, C. Wang, G. M. Odegard and R. Shahbazian Yassar, *Chem. Mater.*, 2014, **26**, 1660-1669.

55. J. Jin, S. Z. Huang, J. Liu, Y. Li, L. H. Chen, Y. Yu, H. E. Wang, C. P. Grey and B. L. Su, DOI: 10.1002/advs.201500070.

Nanoscale Accepted Manuscript